AGU100 ADVANCING EARTH AND SPACE SCIENCE

A Model for the Thermophysical Properties of Lunar Regolith at Low Temperatures

Rachel Woods-Robinson[1,2] (ID), Matthew A. Siegler[3,4] (ID), and David A. Paige[2]

[1]Applied Science and Technology, University of California, Berkeley, Berkeley, CA, USA, [2]Earth, Planetary and Space Sciences, University of California, Los Angeles, Los Angeles, CA, USA, [3]Planetary Science Institute, Tucson, AZ, USA, [4]Department of Earth Sciences, Southern Methodist University, Dallas, TX, USA

Abstract The thermophysical properties of lunar regolith have been thoroughly investigated for temperatures higher than 100 K. For the near-equatorial thermal measurements of the Apollo era, this temperature range was sufficient to generate appropriate models. However, recent measurements from the Lunar Reconnaissance Orbiter Diviner Lunar Radiometer Experiment have revealed polar temperatures as low as 20 K, with apparently lower thermal inertia than explainable by existing theory. In the absence of comprehensive laboratory measurements of regolith thermal properties at low temperatures (<100 K), we investigate solid state theory and fits to lunar simulant materials to derive a semiempirical model of specific heat and thermal conductivity in lunar regolith in the full range 20–400 K. The primary distinctions between these previous models are (1) the temperature dependence of the solid conduction component of thermal conductivity at low temperatures, (2) the focus on regolith bulk density as the primary variable, and (3) the concept that the composition and modal petrology of grains could significantly influence thermal properties of the bulk regolith. This model predicts that at low temperatures, thermal conductivity is as much as an order of magnitude lower and specific heat is likely higher than expected from current models. The thermal conductivity at low temperature should vary depending on the constituent grain materials, their crystallinity, contributions from phonon scattering modes, bulk porosity, and density. To demonstrate the impact of our finding, we extrapolate the effects of our conductivity model on temperature variations in permanently shadowed regions on the Moon. This work motivates experimental confirmation of thermophysical properties of lunar regolith at low temperature.

1. Introduction

The thermal properties of the fine, particulate components of lunar regolith are well understood for temperatures within the range of ~150–400 K. Extensive laboratory tests, in particular, temperature-dependent thermal conductivity and specific heat measurements, have been performed on lunar samples collected from the Apollo and Luna missions (e.g., Cremers et al., 1971a, 1971b; Cremers, 1975; Cremers & Hsia, 1973, 1974; Hemingway et al., 1973; Horai & Fujii, 1972; Horai et al., 1970). Additionally, due to the limited availability of lunar samples, simulant materials have been studied in-depth to better understand thermal transport and characteristics of the lunar regolith (e.g., Fountain & West, 1970). Thermal models based upon these laboratory tests with lunar and simulant regolith are in good agreement with low-latitude, in situ, and orbital remote sensing measurements (Keihm & Langseth, 1973; Vasavada et al., 1999, 2012). Recent reconnaissance of global lunar temperatures, including those in ultracold, shadowed regions, require understanding of thermal properties at lower temperatures.

Specifically, the Lunar Reconnaissance Orbiter (LRO) Diviner Lunar Radiometer Experiment has obtained the first thermal emission measurements in the lunar polar regions. As depicted in Figure 1, these measurements reveal regions in permanent shadow, with temperatures approaching 20 K (Aye et al., 2013; Paige & Siegler, 2016; Paige et al., 2010). These are among the lowest radiometric temperatures measured in the solar system. The interpretation of these recent observations through thermophysical models is relevant for understanding the behavior of lunar volatiles, constraining the thermophysical properties of the lunar regolith at the poles, and measuring the heat flow rate from the lunar interior. To enable more accurate comparisons between thermal model results and observations, we need first to understand the thermal conductivity and specific heat at temperatures down to 20 K. However, these observed temperatures lie in a range in which thermophysical properties of lunar regolith have never been experimentally measured, introducing
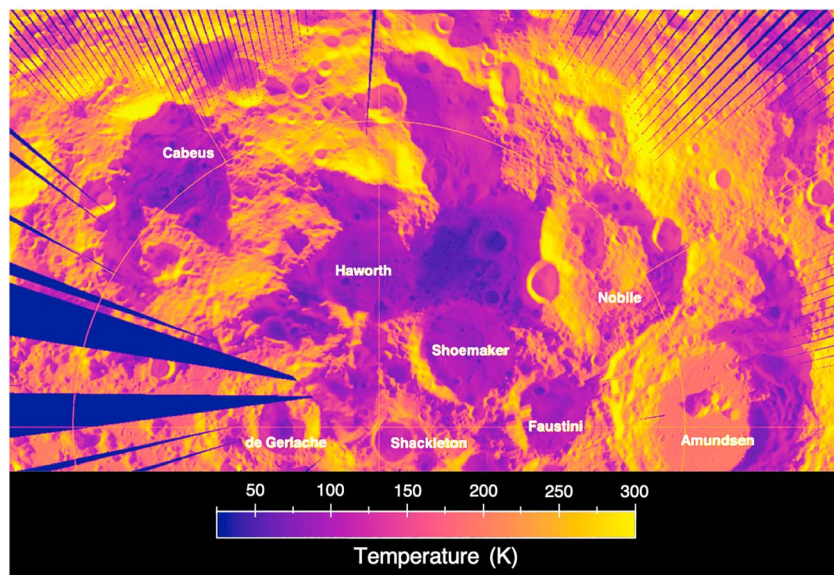
Figure 1. Lunar Reconnaissance Orbiter Diviner thermal image of the south polar region of the Moon showing brightness temperatures as low as 30 K. Winter, nighttime measurements have been found to dip as low as 20 K (Aye et al., 2013; Paige & Siegler, 2016).

a barrier to understanding heat flow. Conventionally, higher temperature measurement trends are extrapolated to low temperature and assumed to hold, but solid state physics suggests that this approach is not physically relevant.

To overcome this barrier using physically relevant techniques, this investigation uses measurements of analog materials and solid state physics principles to derive parameterizations of low-temperature lunar regolith properties that can be used as inputs to lunar thermal models. We extrapolate these to the Moon, adjusting parameters that may differ between laboratory data and in situ lunar measurements. These models are also applicable to cold silicate asteroids and potentially to icy moons, comets, and Kuiper Belt Objects, though few low-temperature laboratory studies of polycrystalline ice thermal properties are present in the current literature.

We first review existing measurements and models for the physical and thermal properties of lunar regolith and simulants. Next, we review the physics of heat capacity and thermal conductivity in solid and particulate materials. We then combine these two frameworks to develop a new approach to model the thermal properties of particulate lunar materials based on bulk density and temperature-dependent functions, and fit these functions to experimental data to estimate the thermal properties at low temperatures. Finally, we demonstrate the impacts of our simplified models on calculated surface and subsurface temperatures.

2. An Overview of Existing Lunar Regolith Measurements and Models

Over the course of 4 years (1969–1972), the Apollo missions collected 2,196 samples (382 kg total) of breccia and basalt rocks and lunar fines (i.e., lunar regolith; Meyer, 2012). Portions of specimens were distributed for analysis to laboratories worldwide, where physical properties—elemental composition, mineralogical and petrological modes, bulk density, particle size distribution, maturity, etc.—were determined, as well as the thermophysical properties of specific heat, thermal conductivity, and thermal diffusivity (Cremers et al., 1971a, 1971b). Samples were typically measured under pressures of or less than 10^{-2} Pa to simulate near-vacuum conditions of the Moon. We now present an overview of the known physical and thermophysical properties of lunar surface regolith, which is the focus material of this study.

2.1. Physical Properties: Composition, Petrology, Particle Size, Bulk Density

"Lunar regolith" is defined here as the fraction of fine material <1 cm in diameter (Lunar Sample Preliminary Examination Team, 1969), but typically refers to particle sizes <1 mm and will be defined as
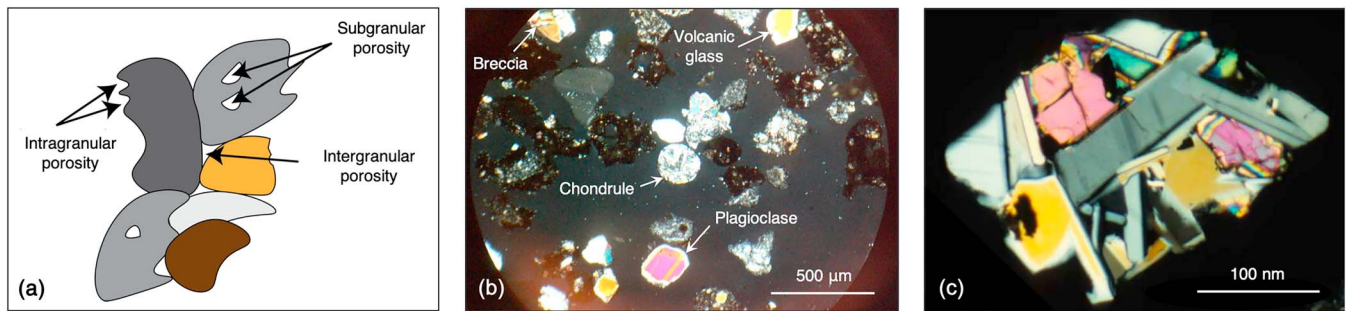
Figure 2. (a) An example schematic of lunar regolith, with colors indicating various particle types. (b) Microscope image of Apollo 16 regolith sample 68501 under cross-polarized light (XPL), consisting of plagioclase feldspar (magenta/yellow twinned grain), volcanic glass (yellow), lunar breccia (dark yellow opaque grains), and a chondrule (round chondrite particle in center consisting of olivine and pyroxene, surrounded by feldspathic mineral). (c) Microscope image of an individual polymineralic grain. Images from (b) and (c) are reproduced with permission from Dr. James L. Berglund.

such in this study. It is dark- to light-gray in color, loose, and clastic. Lunar regolith is derived either from crushed and mixed bedrock (basaltic and anorthositic rock) or meteoritic impact of basaltic rock and coherent microbreccia (Carrier et al., 1973; Heiken, 1975). Its composition can be described by five basic particle types: mineral fragments, pristine crystalline rock fragments, breccia fragments, glasses, and agglutinates (glass-bonded aggregates; McKay et al., 1991). A few major minerals dominate the composition of lunar regolith and rocks: plagioclase, pyroxene, olivine, and ilmenite. These particles and minerals form both homogeneous (monomineralic) and heterogeneous (polymineralic) grains of various sizes and shapes, described subsequently, with subgranular, intergranular, and intragranular porosities. In situ porosity is typically up to 50% for most lunar regolith (Carrier et al., 1991). Figure 2 shows (a) a schematic of a heterogeneous grain containing different types of porosities, (b) a microscope image of a microbreccia regolith sample, containing both monomineralic and polymineralic (breccia and plagioclase) particles, and (c) a higher-resolution microscope image of a polymineralic grain. Color content indicates mineral content from cross-polarized light (XPL).

In general, the compositional and petrologic variations of lunar regolith samples reflect the geological environments of their landing sites. Collected samples are representative of the mare, highland, and intermediate regions (between the mare and highland). For this study, we have

selected seven characteristic surface samples from the "regolith reference suite" (Papike et al., 1982) and summarize their petrologic modes (90–1,000-µm sieve fractions) in Table 1. Studies of these samples reveal the following general trends: mare regolith (Apollo 11 and 12) consist primarily of basalt and mafic minerals like pyroxene and olivine, highland regolith (Apollo 16) contain an abundance of lithic fragments (crushed anorthositic rocks) and plagioclase feldspar, and intermediate regolith (Apollo 15) are a mix of both (McKay et al., 1991).

However, modal composition varies significantly within each region. In this study we will also consider the relative ratio of crystalline components to amorphous components within regolith, which also differs by region. For example, Apollo 11 fines typically consist of a majority of crystalline grains, with fragments of rocks, glass spherules, and glass agglutinates. Apollo 12 fines, on the other hand, contain a chemical composition similar to Apollo 12 breccias but not to single crystalline rocks (Heiken, 1975). Some grains have a fragmental matrix composed of individual minerals (cf. Figure 2c), while others have a crystalline matrix as a result of slow cooling. Another major compositional variant in lunar fines is the glass content, which generally indicates amorphous material. Glass manifests as melt inclusions in crystallized minerals, mesostasis in basalt-based fines, "glass beads" in volcanic breccia-based fines, agglutinates from micrometeorite bombardment (cf. Figure 2d), or as "splash," a thick coating on the surface of rocks (Meyer, 2012). To illustrate the regional variation of amorphous components, glass content was found to range from 50% in Apollo 11 fines to 20% in Apollo 12 fines, and from 10–75% within Apollo 14 samples (Horai & Fujii, 1972).

Table 1
Modal Petrology of Constituent Minerals and Components in the Lunar Regolith Used in This Study, Expressed in Volume Percent (Papike et al., 1982)

Apollo mission	11	12	14	15		16	
Regolith sample	10084	12001	14163	15221	15271	64501	67461
General region	Mare	Mare	Mare-highland	Mare-highland	Mare-highland	Highland	Highland
Specific location	Mare Tranquil-litatis	Surveyor Crater	Fra Mauro Formation	Hadley Region	Hadley Region	Descartes Highland	Descartes Highland
Mineral/ Component							
Lithic fragments	26.3	16.8	16.9	9.4	10.5	17.3	62.4
Mare components							
Mare basalts	24	12.9	2.2	3.1	3.2	0.3	0.5
Highland components							
Anorthosite, norite, troctolite (ANT)	0.4	1	2.9	2.6	2.2	5	21.7
Light matrix breccia (LMB)	0.8	0.1	0.3	0.6	0.4	2.1	30.7
Feldspathic basalt	1.1	0.5	0.6	0.4	1.9	1.6	1.6
Recrystallized noritic breccia/poikilitic breccia (RNB/POIK)	—	2.3	10.9	2.7	2.8	8.3	7.9
Fused regolith components	59.5	49.6	65	50.2	49.9	43	19.6
Dark matrix breccia (DMB)	7.5	9.5	19.3	13.3	12.9	13.9	11.1
Agglutinate	52	40.1	45.7	36.9	37	29.1	8.5
Mineral fragments	7.2	22.4	7.7	29.3	21.2	33.1	13.8
Mafic	4.2	18.3	2.6	16.1	13.5	1	0.5
Plagioclase	1.9	3.9	5.1	13.1	7.4	32.1	12.2
Opaque	1.1	0.2	—	0.1	0.3	—	1.1
Glass fragments	4.8	5.8	4.2	6.7	12.7	3.3	0.5
Orange/black	2.7	0.5	—	0.4	1.6	0.7	0.5
Yellow/green	0.8	2.8	2.9	4.5	7	1.2	—
Brown	—	1.5	—	0.3	0.3	—	—
Clear	1.3	1	1.3	1.5	3.8	1.4	—
Miscellaneous	2.1	5.5	6.1	4.4	5.8	3.4	3.7
Devitrified (crystalline) glass	1.8	5	6.1	4.1	5.6	3.4	3.2
Others	0.3	0.5	—	0.3	0.2	—	0.5
Total	99.9	100.1	99.9	100	100.1	100.1	100
Number of points	625	823	666	1,000	1,008	942	189

Note. Measurements are from the 90–1,000 μm sieve fraction. In the absence of mineral mode measurements for sample 15013, modes of a similar Apollo 15 sample (15020) are given. Two samples from Apollo 15 and 16 are shown to highlight the variation between regolith in the same landing site.

The relative abundance of petrologic and mineralogical modes also depends on particle size. The mean particle diameter of lunar regolith is 40–800 μm, with an average diameter of 60–80 μm (McKay et al., 1991), and particles are typically irregular and elongated (as depicted in Figure 2). Samples in the "regolith reference suite" were sieved into the following size fractions: 90–1,000 μm, 20–90 μm, 10–20 μm, and <10 μm in diameter (Papike et al., 1982). The 90- to 1,000-μm fraction is selected for Table 1 because of its high abundance (35–60% by volume) and ease of petrologic study (petrology of smaller fractions are difficult measure and are typically classified by their chemical composition). Larger clasts tend to be more polymineralic and lithic, while smaller clasts consist of feldspars and glassy phases. Extensive elemental and sieve fraction analyses have been performed in the literature (e.g., Meyer, 2012), but we focus on petrologic modes to highlight the relative ratio between crystalline and amorphous components.

In this study, we aim to parameterize the results of our final model in terms of bulk density. On average, the density of lunar regolith over the entire Moon is approximately 1,500 kg/m^3 (Meyer, 2012) varying from about 1,100 kg/m^3 at the surface to roughly 1,800 kg/m^3 at 1.0-m depth (Hayne et al., 2017). Like other parameters described above, density varies by region; for example, it is looser (~1,500–1,700 kg/m^3) in Apollo 11 fines, more compact (~1,700–1,900 kg/m^3) in Apollo 12 fines, and variable over a wide range (1,280–2,150

kg/m^3) in Apollo 15 regolith (Horai & Fujii, 1972). These regional differences may be explained by regolith layer thickness; the regolith layer at the Apollo 12 landing site is expected to be thinner than at the other sites (Shkuratov & Bondarenko, 2001). Since regolith is compressed in the deeper strata of the lunar surface, bulk density also increases as a function of depth. Bulk density is a function of regolith porosity, so the two parameters can be used interchangeably, and in general grain size has been shown also to increase with depth.

Some one-dimensional thermal models have used a two-layer approximation in which bulk density changes from 1,300 kg/m^3 in the upper regolith to 1,800 kg/m^3 in the deeper regolith (Vasavada et al., 1999). This was found to roughly approximate the surface and subsurface temperatures at the Apollo 17 Heat Flow Experiment site. The upper layer is not necessarily discontinuous (e.g., Keihm, 1984; Vasavada et al., 2012), but near-surface densities are far lower due to micrometeorite overturn of the surface. Fitting Diviner equatorial surface temperature measurements has required a regolith density profile that increases gradually over a depth scale of approximately 6 cm (Hayne et al., 2017; Vasavada et al., 2012).

In summary, lunar regolith is a heterogeneous mixture of particles of various sizes, shapes, and degrees of local heterogeneity (glass beads, rock clasts, agglutinates, etc.), which tend to vary by region. Particles consist of both crystalline and amorphous components. The bulk regolith can be classified in terms of bulk density, porosity, and grain size distribution, which vary with depth. Our model will take these parameters into account to approximate the specific heat and thermal conductivity of lunar regolith.

2.2. Thermal Properties

To understand thermal properties of lunar regolith, we focus on five characteristic "regolith reference suite" samples from Apollo missions 11–16. The temperature-dependent specific heat of lunar material has been measured down to 100 K in the literature using an adiabatic calorimeter (Hemingway et al., 1973; Horai & Fujii, 1972; Robie et al., 1970). As shown in Figure 3a, breccia, vesicular basalt rocks, and lunar regolith from all Apollo missions follow a nearly identical specific heat trend at moderate temperatures of 100–350 K. Thus, considering the wide variation of petrologic modes in Table 1, specific heat appears independent of regolith (or rock) composition, particularly at the lower temperatures. Conventionally, thermophysical models of lunar material fit specific heat measurements to a high-order polynomial. The most recent model to match Diviner (Hayne et al., 2017; Vasavada et al., 2012) data uses a fourth-order polynomial fit to Apollo 12 fines, as motivated by Ledlow et al. (1992):

$$c_{V_0}(T) = c_0 + c_1 T + c_2 T^2 + c_3 T^3 + c_4 T^4 \tag{1}$$

with $c_0 = -5.84 \times 10^4$, $c_1 = 3.64 \times 10^3$, $c_2 = -2.03$, $c_3 = -4.14 \times 10^{-3}$, and $c_4 = 3.87 \times 10^{-6}$ (units inferred, with c_V in units of J·kg^{-1}·K^{-1}) as given in the literature (Hayne et al., 2017; Vasavada et al., 1999). This fit is valid within the range of measurements, as evident in Figure 3a and can be applied generally to all lunar materials in this moderate temperature regime. However, according to this fit the specific heat approaches zero within the range of 20–40 K, which is not physically possible (see section 3.1). Further evidence for the limitations of this fit is provided by nonzero specific heat measurements of Apollo 11 rocks at temperatures less than 5 K (Morrison & Norton, 1970). Thus, applying this fit to thermophysical models in a low-temperature regime will likely yield physically unattainable results.

In the earliest Apollo samples, thermal conductivity of regolith was measured using line heat source techniques or steady state methods (Cremers et al., 1971a, 1971b). More complex methods (e.g., the composite circular cylinder method) were later implemented for revised measurements of lunar core samples (Horai et al., 1980). Thermal conductivity measurements are reported in the range of 100–400 K. Due to a high degree of porosity in regolith, thermal conductivity of lunar regolith is 1–3 orders of magnitude lower than for rocks and thus is conventionally modeled separately from rocks. Figure 3b shows thermal conductivity measurements for our five characteristic samples, with fits described subsequently. Regolith from different regions, presumably with different mineralogical compositions, exhibit distinct conductivity trends. Thus, a simple, general equation for thermal conductivity cannot be derived for all lunar regolith.

Conventionally, thermal conductivity of each specific measurement is fit to an equation referred to in the literature as "Watson's equation" (Watson, 1964):
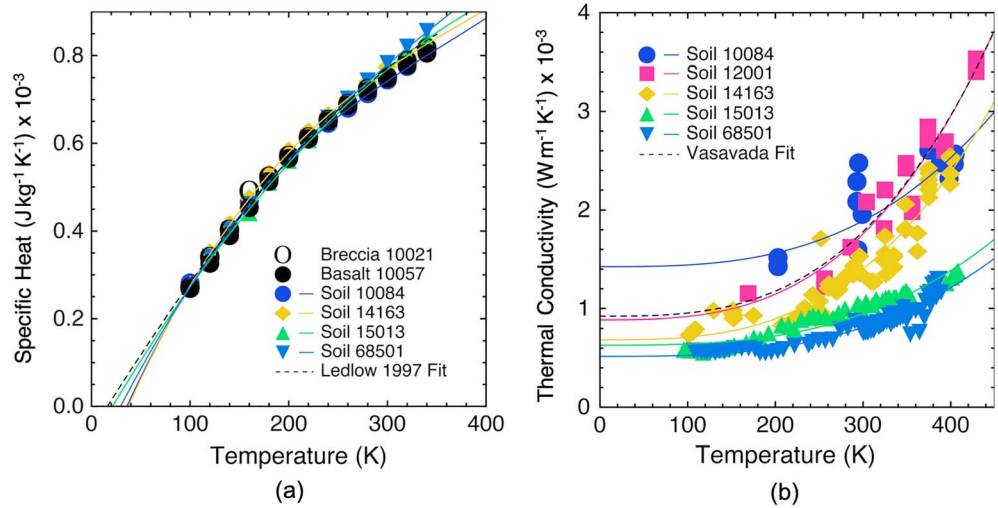
Figure 3. (a) Specific heat measurements (Robie et al., 1970) from Apollo missions fit to the Diviner model (which uses Ledlow et al., 1992) and to the best third-order polynomial fits. (b) Thermal conductivity measurements of regolith (Cremers & Hsia, 1974) fit to Watson's equation (Vasavada et al., 1999; Watson, 1964).

$$k_{\text{eff}_0}(T) = AT^3 + B \qquad (2)$$

where A and B are temperature-independent constants. We will derive and assess this equation later in this study (see section 3.2). Many studies, such as Vasavada et al. (1999), use Watson's equation fit to Apollo 12 regolith with a bulk density of 1,300 kg/m^3 such that $A = 3.18 \times 10^{-11}$ W·m^{-1}·K^{-4} and $B = 9.22 \times 10^{-4}$ W·m^{-1}·K^{-1} to model the top layer of the regolith (Vasavada et al., 1999). Though applicable for 150–350 K (Figure 3b), thermal conductivity may be significantly overestimated at temperatures below 150 K. Heat flow ceases as temperatures approach absolute zero, and all phonon motion ceases (Kittel, 1990), so thermodynamics requires thermal conductivity to approach zero (see section 3.2).

Although not yet measured for lunar regolith, thermal conductivity below 150 K has been studied in other extraterrestrial material. As shown in Figure 4, recreated from Opeil et al. (2010, 2012), a sharp drop in thermal conductivity was found for many meteorite samples when cooled below approximately 150 K. While some samples showed increased conductivity at moderate (50–150 K) temperatures, thermal conductivity universally approaches zero as temperature approaches zero.
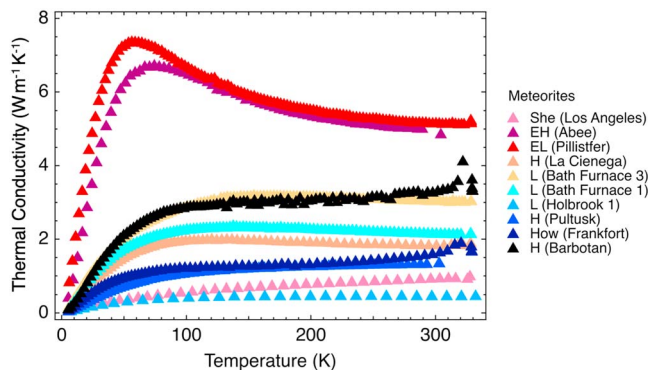

Figure 4. Thermal conductivity versus temperature measurements of a characteristic sample of meteorites from a study by Opeil et al. (2012). This figure has been adapted with permission from Br. Guy J. Consolmagno. The identifying letters in the legend stand for mineral classification: Chondrites (L, H, EL, and EH), Howardites (How), and Shergottites (She).

In Figure 4, each sample has a very distinct thermal conductivity versus temperature profile, with thermal conductivities lower than expected from simply averaging their constituent minerals. In particular, the EL (Abee) and EH (Pillistfer) samples rise to a peak near ~50 K and then decrease as a temperature increases. Other samples have a broader peak between 50 and 150 K, and some increase monotonically. The differences in each profile are likely due to variations in sample composition and porosity (i.e., density) within these meteorite samples. An inverse relationship between thermal conductivity and porosity was mentioned by Opeil et al., but an in-depth understanding of the trend and the existence of peaks is not provided. In comparison to meteoritic rocks, planetary regolith—transformed by slow, steady impact gardening—should exhibit similar variations in thermal conductivity versus temperature profiles with packing density, composition, and crystallinity.

2.3. Lunar Regolith Simulants

Specific heat measurements in the temperature range from 100 to 350 K show little variability between lunar samples (cf. Figure 3), so it is reasonable to assume that variations in bulk density and composition do not
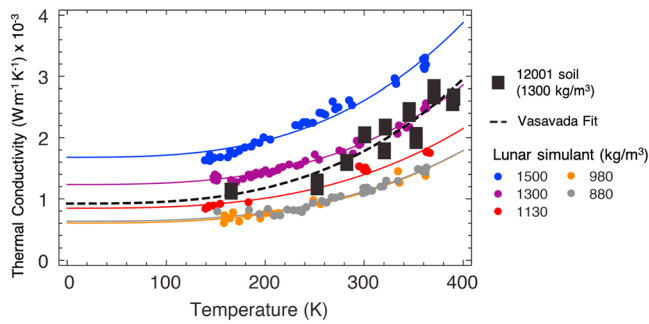
Figure 5. Thermal conductivity measurements of various densities of basalt-based lunar regolith simulant as a function of temperature, reproduced from Fountain and West's (1970) study. Fits are from Watson's equation (equation (2)). Apollo 12 regolith sample 12001 fit to Vasavada et al. (1999) equation, which is derived from Watson's (1964) equation, is shown for comparison.

contribute significantly to the specific heat. However, this assumption does not apply to thermal conductivity. Due to variability in both the composition and the density between each lunar regolith sample, one cannot easily isolate the effects of bulk density in thermal conductivity measurements from Figure 3b.

In order to study the effects of bulk density on thermal conductivity, we will examine thermal measurements of lunar regolith simulants from the literature. Lunar simulants are synthesized to approximate the chemical composition, mineralogy, particle size, specific gravity, etc., of lunar regolith (Willman et al., 1995), and are advantageous for this application for a number of reasons. Apollo samples are a limited resource so simulants allow more comprehensive studies. Furthermore, simulant material allows for isolation of a single variable, such as bulk density, while keeping constant other parameters, such as particle size or petrologic mode. Furthermore, there is disagreement in the literature about the correct value of bulk densities of Apollo samples, with ambiguity resulting from different experimental and handling procedures, so simulants can provide a higher degree of accuracy.

We select measurements from Fountain and West's (1970) investigation of a particulate basalt lunar simulant, which aimed to provide data for future mathematical models. Lunar-like terrestrial basalt was crushed to powder form and compressed in a powder pellet press to achieve densities ranging from 790 to 1,500 kg/m^3 (for comparison, the density of solid basalt is about 2,400–3,100 kg/m^3). Samples were sieved to 37- to 62-μm diameter, slightly below average size for lunar regolith, and particle size was held constant for each density. With these samples, thermal conductivity was measured as a function of bulk density in simulated lunar environments of 10^{-6} Pa in a temperature range 135–370 K (cf. Figure 5). Data are fit by Fountain and West using Watson's equation (equation (2)) and, as described above, the fit below 100 K is not physically relevant. While these measurements may be overly idealized and thus not directly applicable to in situ lunar regolith, they offer a consistent density dependence that cannot be achieved with actual lunar regolith (cf. Figure 3b to Figure 5).

Although measurements were not performed below 100 K, to our knowledge no other experimental studies exist in the literature that measure thermal conductivity of lunar or simulant particulate material at various bulk densities while keeping other parameters constant. Thus, data from this study provide the best experimental framework upon which to base our model for thermophysical properties in the "low-temperature regime" of 20–100 K.

3. Solid State Heat Transfer

To understand how heat flows through particulate material in the lunar regolith, we will review the mechanisms of heat transfer in solids and then consider regolith particles as conglomerates of solid constituents. Lattice vibrations, quantized as phonons, dominate the thermal properties of the electrically insulating and dielectric solids present in lunar minerals (Ashcroft & Mermin, 1976; Kittel, 1990), while electronic effects are negligible. This section will consist of brief derivations of temperature-dependent specific heat and thermal conductivity in solids. We will focus on the differences in thermal properties between crystalline and amorphous solids and semiempirical methods that relate properties of particulates to those of solids. Then, we will use this understanding to derive a semiempirical equation for effective conductivity within lunar regolith.

3.1. Specific Heat
3.1.1. Solids

Heat capacity measures the ability of any material to store thermal energy. Quantitatively, heat capacity measures the amount of thermal energy Q required to change the temperature T of a material by a given amount (conventionally, by 1 K). This property is intrinsically expressed as specific heat capacity c, that is, heat capacity per unit mass, is independent of the size of a system, and is given in SI units J·kg^{-1}·K^{-1}:

$$c = \frac{1}{m}\left(\frac{\delta Q}{\delta T}\right) \tag{3}$$

The intrinsic property c is a function of atomic and molecular structure and m is the molecular mass. Solid materials can store energy in translational, rotational, vibrational degrees of freedom, and in outer shell atomic electrons. In crystalline solids, classical statistical mechanics and the equipartition theorem give rise to a temperature-independent specific heat, known as the Dulong-Petit law:

$$c = \frac{3R}{M} \tag{4}$$

where R is the universal gas constant and M is molar mass (Ashcroft & Mermin, 1976; Dulong & Petit, 1818; Kittel, 1990). Experimentally, it has been shown that the specific heat of solids approaches a limit near the Dulong-Petit value at high temperatures, but at low temperatures a very different trend occurs: in crystalline solids specific heat decreases monotonically to zero, and at very low temperatures ($\sim < 2$ K) it is proportional to T^3 as shown by Debye (Kittel, 1990).

An explanation of this T^3 behavior required the development of quantum mechanics. Atoms need a minimum "quanta" of available energy to essentially activate each degree of freedom and make it accessible to store energy. This energy is manifested in the form of kinetic energy or temperature. As temperature drops, some of the degrees of freedom accessible at higher energies become unattainable and are "frozen out." Thus, the specific heat approaches zero at absolute zero, where no degrees of freedom are available.

Albert Einstein initially recognized the quantization of atomic vibrations and proposed a model of solids that considered atoms as 3-D quantum harmonic oscillators of uniform frequency (Einstein, 1907). Einstein's model approached the Dulong-Petit limit but at low temperatures decreased exponentially and significantly underestimated experimental specific heat in crystalline solids (Eucken, 1911). Peter Debye discerned that the number of vibrational modes in a solid is finite, and modified Einstein's model by considering lattice vibrations as nondispersive phonons in a box, including both longitudinal and transverse standing waves (Debye, 1912). By proposing a maximum phonon frequency ν_D, introducing a Debye temperature $\theta_D = \frac{h\nu_D}{k}$, where h is Planck's constant, k is Boltzmann's constant, noting that phonons follow Bose-Einstein statistics, he derived the following expression for specific heat (per volume):

$$c_v = \frac{12\pi^4}{5}N_A k\left(\frac{T}{\theta_D}\right)^3 \tag{5}$$

This model correctly predicts the observed T^3 behavior of specific heat of crystalline solids at cryogenic temperatures and approaches the Dulong-Petit limit at high temperatures (for good electrical conductors, an additional electronic component $c_e = AT$ is added). Comprehensive derivations are outlined in standard textbooks (Ashcroft & Mermin, 1976; Kittel, 1990).

Due to simplifying approximations, in particular the inverse proportionality of phonon frequency and wavelength, the Debye model is inconsistent at intermediate temperatures between cryogenic temperatures and the Dulong-Petit limit. Deriving an accurate model in this regime is nontrivial. Various corrections have been applied to the Debye model, but usually, specific heat is treated on a case-by-case basis and fit to experimental data. Many measurements for insulating solids have shown the intermediate temperature trend to be roughly linear, though this differs by material (Simon, 1922).

Amorphous or glassy solids typically follow an identical high-temperature trend as crystalline solids of the same chemistry, but diverge at low temperatures. Phonon scattering experiments revealed Einstein's model as more accurate than Debye's for describing the specific heat of amorphous solids (Cahill & Pohl, 1988). As an example, crystalline and amorphous SiO_2 (quartz) exhibit a near-exact specific heat behavior as evident in Figure 6b. Below 100 K, amorphous SiO_2 has a higher specific heat, likely due to additional localized modes of the disordered amorphous state (Zeller & Pohl, 1971). This difference is most significant below around 10 K, though nonzero in the range 10–100 K. Despite these slight discrepancies, the specific heat of all solid dielectrics and insulators follow very similar temperature dependencies, with T^3 proportionality at low temperatures and a near-constant value at high temperatures.
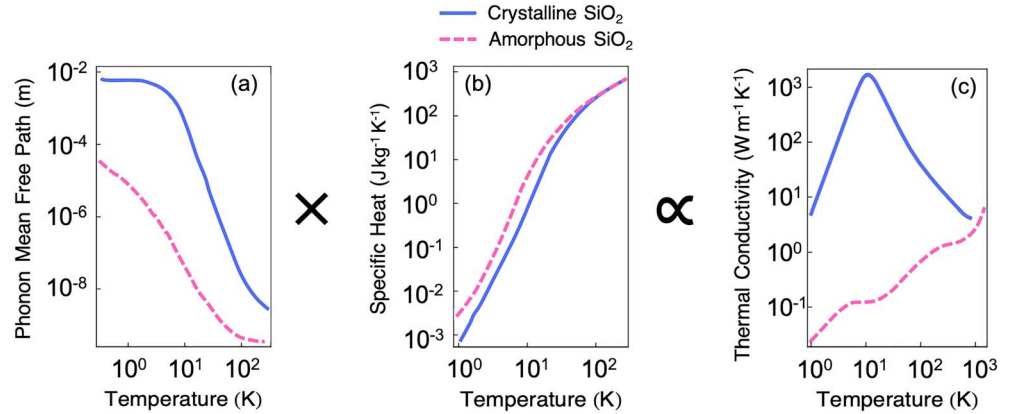
Figure 6. Graphical illustrations of the Debye relation, $l\,c_V \propto k$, for representative samples of crystalline (blue, solid) and amorphous (pink, dotted) SiO$_2$, with (a) mean free path (Cahill & Pohl, 1988), (b) specific heat (Cahill & Pohl, 1988; Zeller & Pohl, 1971), and (c) thermal conductivity (Touloukian & Ho, 1970) as functions of temperature. In this schematic, the product of (a) and (b) is multiplied by a constant (the phonon velocity) to produce (c). The crystalline phase plotted here is α-phase cristobalite. Note the logarithmic scale of both axes.

3.1.2. Particulates

The specific heat of particulate and porous materials can be modeled as a function of specific heat of the constituent solid(s). In homogeneous particulate material, heat capacity—and, by extension, specific heat capacity—of particulates is directly proportional to the porosity-free value, $c_{\text{solid}}(T)$ (de Vries, 1963):

$$c_{\text{soil}}(T) = \frac{\rho_{\text{solid}}}{\rho_{\text{bulk}}} c_{\text{solid}}(T) \tag{6}$$

Though this model is adapted from studies of terrestrial regolith, it can be applied to regolith in a vacuum by replacing liquid and gas components in pores with vacuum. For heterogeneous regolith, (6) becomes a weighted sum of the specific heats of the solid constituents (Campbell & Norman, 1998):

$$c_{\text{soil}}(T) = \frac{\sum_i \rho_i v_i c_i(T)}{\rho_{\text{soil}}} \tag{7}$$

where index i refers to a solid component of the composite material, ρ_i to its density, v_i to its volumetric contribution, and $c_i(T)$ to its solid state heat capacity.

It is important to note that this method models the specific heat at constant volume of particulate material. Experimental calorimeter readings, on the other hand, measure the specific heat at constant pressure. For all practical purposes in the low to moderate temperature regime, the difference between these two values is negligible and herein in this study $c_{\text{soil}} \approx c_V \approx c_P$ (Leadbetter & Morrison, 1963).

3.2. Thermal Conductivity
3.2.1. Solids

Thermal conductivity is closely related to specific heat. While specific heat expresses the ability of a material to store energy, thermal conductivity expresses the ability of a material to exchange this energy with its surroundings. It is measured in units of power per distance per temperature (W·m^{-1}·K^{-1} in SI units) and is typically evaluated from Fourier's law of heat conduction (Fourier, 1878), expressed in three dimensions as follows:

$$q = -k\nabla T \tag{8}$$

where q is heat flux, k is thermal conductivity and ∇T the temperature gradient or differential.

Debye's elastic wave theory applies the kinetic theory of gases to solids, deriving the following relation between thermal conductivity, specific heat c_v, phonon velocity v, and phonon mean free path l (Debye, 1912):
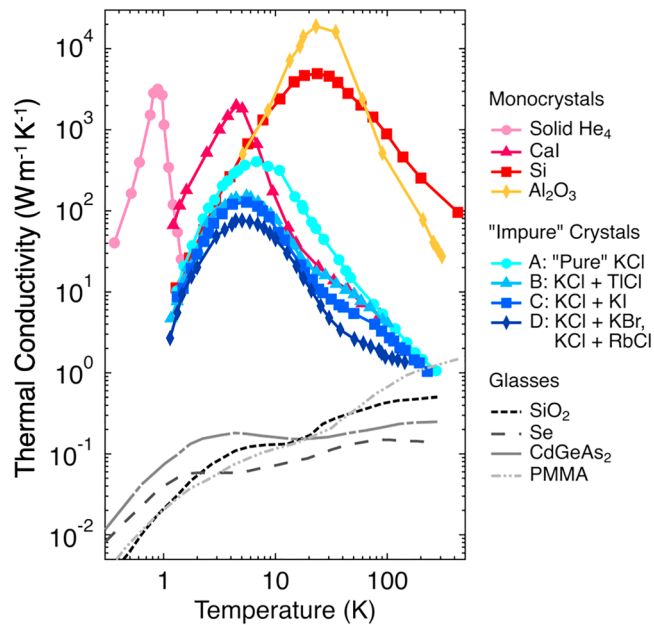
Figure 7. The temperature dependence of thermal conductivity in various solids, adapted from Cahill & Pohl, 1988. Monocrystalline "pure" solids have a peak due to Umklapp scattering, and the low-temperature tails are affected by crystal boundary scattering. Peak locations and amplitudes are determined by material properties. Defect-rich, or "impure" crystalline materials are additionally affected by impurity scattering. In contrast, amorphous solids (glasses) exhibit a variety of scattering mechanisms and are several magnitudes less conductive than crystalline solids (Cahill & Pohl, 1988). A, B, C, and D refer to "pure" KCl, KCl + TlCl ~ 7×10^{18} cm^{-3}, KCl + KI = 1.25×10^{19} cm^{-3}, and {KCl + KBr = 1.6×10^{20} cm^{-3}; KCl + RbCl = 1.5×10^{20} cm^{-3}}, respectively.

$$k = \frac{1}{3} c_V v \mathrm{l} \qquad (9)$$

This relation is depicted graphically in Figure 6 for crystalline and amorphous SiO$_2$. Assuming a negligible change in phonon velocity with temperature, this equation implies that thermal conductivity is proportional to the product of a material's specific heat and mean free path. Though the specific heats of various solid materials follow a similar temperature dependence at intermediate to high temperatures (>100 K), thermal conductivity of the same materials can differ by orders of magnitude. This is due primarily to the dependence on mean free path (Figure 6a), which is inversely proportional to the phonon scattering probability and thus a function of molecular structure, crystal purity, crystal size, and kinetic energy (i.e., temperature). We will explain three exemplary cases.

First, in monocrystalline ("pure") defect-free solids, the dominant phonon scattering mechanism is typically Umklapp scattering, in which two phonons scatter inelastically off of one another. The rate of scattering depends on the thermal population of phonons, such that phonon scattering increases exponentially (i.e., mean free path decreases exponentially, cf. blue curve, Figure 6a) with increasing temperature (Cahill & Pohl, 1988). At a critical temperature, this drop in mean free path contributes more significantly to the thermal conductivity than the increase of specific heat (blue curve, Figure 6b). Thus, thermal conductivity of crystalline solids increases to a peak and then decreases monotonically with increasing temperature (blue curve, Figure 6c). The location and height of this peak is characteristic of each crystalline material and is a function of chemical composition, structure, and bonding. These fluctuations are depicted at the top of Figure 7, plotting thermal conductivity of various crystalline materials over several magnitudes of temperatures.

Second, for our purposes we will classify defective crystals as containing either chemical (i.e., intrinsic defects or extrinsic dopants) or physical (e.g., polycrystals) impurities. In this class, which makes up the majority of real crystals, phonon deflection off of lattice defects becomes a dominant scattering mechanism. For chemical defects this scattering typically occurs via three processes: mismatch scattering, the isotope effect, and scattering by impurity modes (Cahill & Pohl, 1988). These processes essentially result in a similar effect: the peak in thermal conductivity occurs at the same temperature as it would in a monocrystalline solid of the same chemistry, but its magnitude is damped as crystal purity decreases. The middle section of Figure 7 demonstrates this phenomenon in KCl crystals. For physically defective (e.g., polycrystalline or nanocrystalline) materials, the scattering of elastic waves off of defects and/or grain boundaries gives rise to additional resistance and similarly damps the phonon mean free path, and thus the thermal conductivity (Casimir, 1938). This damping effect appears more prominent at very low temperatures (typically <5 K), where the mean free path would approach macroscopic lengths if not limited by scattering off of boundaries and defects.

Third, amorphous materials have a distinct thermal conductivity versus temperature relation. Due to a high degree of lattice disorder, phonon scattering probability is orders of magnitude greater in amorphous materials than in crystalline materials (i.e., mean free path is orders lower, cf. pink curve in Figure 6a). The thermal conductivities of various amorphous compounds are plotted in the bottom of Figure 7 (note: logarithmic axes). Above approximately 30 K the mean free path approaches interatomic spacing, so phonon heat transfer becomes negligible and thermal properties are well characterized through random walk statistics of Einstein's model. Because the mean free path is so small, its effect on thermal conductivity is negligible and the specific heat dominates. Thus, the thermal conductivity increases, reaches a "plateau" (or a slight peak) around 2–10 K where the mean free path derivative is maximized, and then continues to increase monotonically. Unlike crystalline materials, temperature

dependence of thermal conductivity in many amorphous solids has nearly the same trend and is essentially independent of chemical composition and bonding (cf. Figure 6c and bottom of Figure 7; Zeller & Pohl, 1971). Furthermore, thermal conductivities are several orders of magnitude lower than those of crystalline materials.

The two distinct temperature-dependent profiles are present in almost all crystalline and amorphous materials, which account for all constituents of lunar regolith, though certain anomalies have been found to occur. Certain types of disorder or symmetry breaking in solid crystalline materials can act as strong phonon scatters and lead to glass-like lattice vibration (Cahill & Pohl, 1988). One such anomaly of particular importance to this study occurs in feldspar. Surprisingly, the thermal conductivity of various crystalline feldspar minerals increases monotonically with temperature in a manner similar to amorphous solids (Birch & Clark, 1940). We also caution that discerning locally disordered crystalline solids and amorphous solids is not always straightforward. With small enough particle size and significant grain boundary scattering, the crystalline thermal conductivity trend can be reduced to the amorphous trend. However, we have shown in general that the thermal physics in crystalline and amorphous solids is quite different, primarily due to the scattering mean free path.

3.2.2. Particulates

Heat transfer occurs through three dominant mechanisms: conduction, convection, and radiation. In bulk solids at moderate temperature, heat is transferred through conduction only, as described in the previous section. In particulate material, radiative transfer and convective transfer become significant. Effective thermal conductivity k_{eff} can be expressed as the sum of the three primary heat transfer mechanisms (Wechsler et al., 1972), such that

$$k_{\text{eff}} = k_c + k_g + k_r \tag{10}$$

where k_c, k_g, and k_r are components due to conduction, gas convection, and radiation mechanisms. At terrestrial, and even Martian, atmospheric pressures, the gas convection term k_g dominates and k_{eff} can be expressed as resistors in parallel (Kannuluik & Martin, 1933). Various studies have shown k_g to decrease with decreasing pressure (Wechsler & Glaser, 1965) and to become negligible below approximately 10^{-2} Pa. This range applies to the near-vacuum conditions of the Moon, so thermal conductivity of lunar regolith in near vacuum can be simply expressed as

$$k_{\text{eff}} = k_c + k_r \tag{11}$$

that is, the sum of a conduction component and a radiative component (Wechsler et al., 1972). This k_r term is proportional to T^3, especially above 250 K in vacuum, leading to Watson's equation (equation (2)).

3.2.3. Conduction Component Density Dependence

In particulate material, there exist two primary mechanisms of conductive transfer, represented by the terms k_c (or B in Watson's equation, equation (2)). The first mechanism occurs within solid particles by phonon conduction, electron conduction, or thermal radiation. The second occurs across interparticle contacts. Simplistically, conduction across grains in homogeneous regolith can be described as the solid conduction of the grain dominated by the bottleneck of resistance at the grain contacts. Various formulae have been derived to describe conduction in near-vacuum regolith and are reviewed by Merrill (1969), among others. The following density-dependent formula was derived by Halajian et al. (1967):

$$k_c = b(1-p)\left[\frac{\pi \rho g \left(1-\nu^2\right)}{E} k_{\text{solid}}\right]^{1/3} z^{1/3} \tag{12}$$

where p is porosity, ρ bulk density, g gravitational acceleration, ν Poisson's ratio, E the modulus of elasticity, z the depth of the regolith, and b a constant. Although this model assumes $k_c \propto \rho^{1/3}$, other models in the literature claim various density dependences, typically $k_c \propto \rho^n$ (Merrill, 1969). Since we are interested only in the variables of bulk density ρ and porosity p to build a simple model, for our purposes we absorb other variables into a constant. We also make this assumption that z is a function of ρ and absorb regolith depth z into an unknown ρ-dependent function $b(\rho)$. Thus, equation (12) can be simplified as follows:

$$k_c = (1-p)\, b(\rho)\, k_{\text{solid}}(T) \qquad (13)$$

where $b(\rho)$ is the unknown bulk density-dependent function and $k_{\text{solid}}(T)$ is the temperature-dependent conductivity of the bulk solid component. Porosity is a function of bulk density ρ and solid density ρ_{solid} (i.e., the density of an individual grain):

$$p = 1 - \frac{\rho}{\rho_{\text{solid}}} \qquad (14)$$

3.2.4. Temperature Dependence
In the planetary science literature, temperature dependence of k_c for regolith in vacuum is evaluated by the following three approaches (Presley & Christensen, 1997; Wechsler et al., 1972):

$$k_c = \begin{cases} B & \text{(i) Negligible temperature dependence} \\ B + CT & \text{(ii) Glasses and silicates} \\ B + CT^{-1} & \text{(iii) Crystalline materials} \end{cases} \qquad (15)$$

The conduction component is conventionally taken as (i), which is equivalent to k_c in Watson's equation (Watson, 1964). Temperature-independent k_c is a reasonable approximation for the moderate temperature regime ($\sim >100$ K), since, as shown in the previous section, the intrinsic thermal conductivity of solids in this range is nearly constant (Presley & Christensen, 1997). However, in the low-temperature regime k_c will approach a steeper temperature-dependent gradient and (i) becomes invalid.

Thermal conductivity in amorphous solids is roughly linear at low temperature so (ii) is approximately valid. However, (iii) is only a valid approximation so long as the peak from Umklapp scattering onset occurs below the lowest temperature in the range of interest. Although the literature mentions equation (15), there are no instances of fitting data to (ii) and (iii), and most models assume (i) because it is adequate in the moderate temperature regime (Wechsler et al., 1972). Our study will differ from other studies by revising (ii) and (iii) within the framework of equation (13) to be consistent with solid state conductivities from Figures 6 and 7.

3.2.5. Heterogeneous Regolith
Additionally, when regolith particles are composed of multiple constituents (polymineralic grains or mixed grains of various compositions), the conduction term becomes a function of the solid conductivity of each constituent. Thermal conductivity of two-phase and three-phase heterogeneous mixtures of solids, suspensions, emulsions, porous material, etc., have been studied extensively by various authors (e.g., Cheng & Vachon, 1969; Hamilton & Crosser, 1962). Heterogeneous two-phase models consider phases thermally in series or in parallel with respect to heat flow. Phases thermally in series gives a lower limit estimate:

$$k_{\min} = \frac{k_1 k_2}{v_1 k_2 + v_2 k_1} \qquad (16)$$

Phases thermally in parallel gives an upper limit estimate:

$$k_{\max} = v_1 k_1 + v_2 k_2 \qquad (17)$$

Other models consider some combination of both (Woodside & Messmer, 1961), where k_1 and k_2 represent the thermal conductivity of the two phases, and v_1 and v_2 are the volume fractions of each component. It is conventional for liquid phases to be considered in series and solid phases considered in parallel, so for the context of this study in the absence of liquid we can approximate k_c with the parallel approach. Note that this assumption may break down at higher temperatures with the incorporation of liquid phases, though at that point radiation will likely dominate (Merrill, 1969). As in equation (6), we must also multiply each component by ρ_i/ρ to account for porosity in the sample. Effectively, in heterogeneous regolith the solid conductivity factor can be replaced with

$$k_{\text{solid}}(T) \rightarrow \frac{\sum_i \rho_i \nu_i k_i(T)}{\rho} \tag{18}$$

Substituting equation (18) into equation (13) and absorbing $1/\rho$ into the function $c(\rho)$, we estimate the conduction component as

$$k_c = c(\rho)(1-p)\sum_i \rho_i \nu_i k_i(T) \tag{19}$$

3.2.6. Radiative Component

Experimental and theoretical studies have shown the radiative component of thermal conductivity to be the dominant heat transfer mechanism for particulate material in vacuum at moderate temperatures (Merrill, 1969). Radiative transfer occurs primarily across and between void spaces. It also occurs within particles, but the latter mechanism is typically negligible compared to the former (Wechsler et al., 1972). To understand the source of the T^3 dependence in Watson's equation (equation (2)), we walk through the derivation.

Nearly all derivations of the radiative component in the literature emanate from two assumptions: uniform temperature within particles ($\Delta T_{\text{particle}} \ll \Delta T_{\text{surroundings}}$) and high opacity of particles to thermal radiation (Merrill, 1969). From the Stefan-Boltzmann law, the power q_x radiated in one dimension between two idealized particles with different temperatures T_1 and T_2, constant emissivity ϵ, and separated by distance δx, can be expressed as

$$q_x = F_G \sigma \epsilon \left(T_1^4 - T_2^4\right) \tag{20}$$

where σ is the Stefan-Boltzmann constant and F_G a dimensionless constant based on particle geometry. Assuming $T = T_2 \approx T_1$ and $\delta T = T_2 - T_1$ is very small, a first-order expansion reduces equation (20) to

$$q_x = 4F_G \sigma \epsilon T^3 \delta T = 4F_G \sigma \epsilon T^3 \delta x \left(\frac{\delta T}{\delta x}\right) \tag{21}$$

Fourier's law in one dimension is expressed as

$$q_x = -k_r \left(\frac{\delta T}{\delta x}\right) \tag{22}$$

where k_r is the effective thermal conductivity due to radiative transfer. By combining equations (21) and (22), the radiative component of thermal conductivity k_r can be derived as (Schotte, 1960)

$$k_r = 4F_G \sigma \epsilon \delta x T^3 \tag{23}$$

This is the model used by Watson, with all temperature-independent variables absorbed into a constant A such that $k_r = AT^3$ as in equation (2). Watson suggests that A is proportional to density (Watson, 1964). While other studies include a porosity-dependent term (Laubitz, 1959; Merrill, 1969; Russell, 1935), we do not include this in our model. Since bulk density is a function of porosity, this study will replace A with an unknown bulk density-dependent function $a(\rho)$ to account for density dependence, such that

$$k_r = a(\rho)T^3. \tag{24}$$

Substituting both the conductive component (equations (18) and (19)) and radiative component (equation (24)) into equation (11) gives the following relations for homogeneous (equation (25)) and heterogeneous (equation (26)) particulate material:

$$k_{\text{eff}}(T,\rho,p) = a(\rho)T^3 + c(\rho)(1-p)\,k_{\text{solid}}(T) \tag{25}$$

$$k_{\text{eff}}(T,\rho,p) = a(\rho)T^3 + c(\rho)(1-p)\sum_i \rho_i \nu_i k_i(T) \tag{26}$$

4. A Two-Component Linear Combination Model

4.1. Concept

Lunar regolith contains a large number of constituents in various orientations, as demonstrated by Figure 2 and Table 1. Thus, the collective thermal properties of lunar regolith will include contributions from all constituents. As a first-order approximation in our model, we reduce solid components to a linear combination of two "generic" solids: a crystalline-like solid and an amorphous-like solid. Crystalline α-phase cristobalite SiO_2 and amorphous SiO_2 are selected as the two "generic" solids and the two building blocks for our model.

Essentially, any two solids illustrating the prototypical crystalline and amorphous thermal conductivity trends outlined in section 3.2.1 could be used, but these materials are selected for (1) their prevalence in the literature, (2) their precise and accurate measurements down to the low-temperature regime, and (3) the prominence of silicates in the lunar regolith. Amorphous SiO_2, that is, glassy silica, has been shown to follow the thermal conductivity trend characteristic of nearly all amorphous materials (cf. section 3.2), so this choice is reasonable as a "generic" amorphous solid. The temperature versus thermal conductivity relation for crystalline α-phase SiO_2, our "generic" crystalline solid, shows the Umklapp peak and subsequent decrease of thermal conductivity typical of crystalline solids (cf. Figure 6). To adjust this relation for different crystalline materials, the peak can be dampened and shifted in the model by applying a transformation function. This general principle of superposing two solid components is applied to model both specific heat and thermal conductivity, using the equations derived in section 3.

Before deriving the models, an even further simplification will be introduced. Our "zeroth-order approximation" assumes that the amorphous component dominates and that the crystalline component is negligible. This assumption is justified in part because of the increase in grain boundary scattering when the particle size is decreased (leading toward a drop in long-range order). Additionally feldspar, one of the dominant crystalline mineral modes in the regolith (cf. Table 1), demonstrates amorphous-like thermal conductivity trend rather than crystalline-like (Birch & Clark, 1940). Our initial model will use this assumption, and then we will introduce a crystalline component as a sensitivity analysis.

4.2. Specific Heat Model

From equation (7), the specific heat of particulate material is the sum of the specific heats of constituent solid components normalized by their volume fraction and density, so

$$c_V(T) = \frac{d(\rho)}{\rho} \left[\rho_{cr} v_{cr} c_{cr}(T) + \rho_{am} v_{am} c_{am}(T) \right] \tag{27}$$

where $c_{cr}(T)$ and $c_{am}(T)$ are the specific heat of the crystalline and amorphous "generic" solids, ρ_{cr} and ρ_{am} are their densities, v_{cr} and v_{am} are their volumes, and ρ is the bulk density of the heterogeneous regolith. A damping function $d(\rho)$ is added to aid in fitting and to account for uncertainties in this approximation.

Since each of the two phases is essentially a mean value of many materials, solid densities ρ_{cr} and ρ_{am} are averaged values of many material densities. Thus, for this simplistic model they are considered equivalent in both crystalline and amorphous components. Densities ρ_{cr}, ρ_{am}, and ρ are absorbed into the damping coefficient. However, as demonstrated previously specific heat of lunar regolith does not change significantly with bulk density, so we will assume $d(\rho)$ to be ρ-independent and reduce to a damping coefficient, d_c. The volume fraction of crystalline particles v_{cr} is given the variable x. With only two phases, the amorphous volume fraction v_{am} is $(1 - x)$. Thus, we have the following equation:

$$c_V(T, x) = d_c [x c_{cr}(T) + (1-x) c_{am}(T)] \tag{28}$$

For our two-component linear combination model, the functions $c_{cr}(T)$ and $c_{am}(T)$ are fits to the temperature-dependent specific heat measurements of α-cristobalite SiO_2 and amorphous SiO_2, respectively (Simon, 1922; Zeller & Pohl, 1971). To most accurately capture behavior at low temperatures, we fit experimental data to sixth-order polynomial piecewise functions, divided into a low-temperature regime (35–100 K) and an ultralow temperature regime (5–35 K) portions.
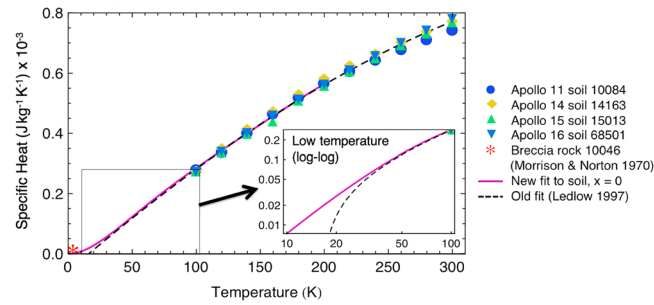
Figure 8. Revised estimate of the specific heat versus temperature of lunar regolith from the "zeroth-order approximation" (equation (29)). This estimate is valid in range 10–400 K. The new model applies below 200 K and the old model (equation (2)) applies above 200 K. The measurement of a breccia rock at cryogenic temperatures has been shown for comparison (Morrison & Norton, 1970).

To introduce the zeroth-order approximation, we let $x = 0$ such that the only unknown is the coefficient d_c. The measured specific heat of regolith sample 10084 from Apollo 11 (Robie et al., 1970) is fit within the temperature range of 10–200 K to equation (28) to give a damping coefficient of $d_c = 1.04$. This indicates that the number of available modes of vibration in particulate material is approximately equal to that of the generic amorphous solid. The value of the damping coefficient may indeed be slightly greater than unity due to additional vibrational modes (Zeller & Pohl, 1971).

The following piecewise function is derived for estimating the specific heat of fines in the lunar regolith:

$$c_V(T) = \begin{cases} aT + bT^2 + cT^3 + dT^4 + fT^5 + gT^6 & 10\text{K} < T < 200\,\text{K} \\ C_{V_0}(T), & 200\text{K} < T < 400\;\text{K} \end{cases} \quad (29)$$

with $a = -1.12 \times 10^{-1}$, $b = 9.62 \times 10^{-2}$, $c = -1.26 \times 10^{-3}$, $d = 7.69 \times 10^{-4}$, $f = -2.37 \times 10^{-8}$, and $g = 2.84 \times 10^{-11}$ (units inferred, with c_V in units of J·kg^{-1}·K^{-1}).

At temperatures 200–400 K, the function $c_{V_0}(T)$ is retained from previous models (cf. equation (1)). This piecewise function is plot with experimentally measured specific heat in Figure 8. In the range 50–200 K, the new model is relatively consistent with the old model. However, below 50 K the new model estimates specific heat values significantly higher than previously predicted. Around 20 K, the specific heat from this model is approximately 27 J·kg^{-1}·K^{-1}. This is about twice as high as the previous model predicted (14 J·kg^{-1}·K^{-1}), and thus regolith should lose heat less readily than expected in previous models. It must be noted that this model is only applicable down to ~10–15 K, where the Schottky anomaly occurs (Zeller & Pohl, 1971). To date there are no experimental measurements to validate this model, but the average specific heat of a breccia rock at 3–4 K from Morrison and Norton's (1970) study is plotted in Figure 8 for reference. Their measured value of approximately 4.2 J·kg^{-1}·K^{-1} is about 4 times higher than this model predicts (10^{-3} J/g-K), but the temperature they measured lies outside the range of accuracy and an updated model is required to fit to this scale.

As a sensitivity analysis to assess the degree to which grain crystallinity influences specific heat of regolith material, x in equation (28) is varied incrementally from 0 to 1. The result is a dip toward slightly lower specific heats with increasing crystallinity, as shown in Figure 9a; at the limit of $x = 1$ at ~20 K, specific heat is less than half as much as $x = 0$ at the same temperature. Thus, the accuracy of applying the zeroth-order approximation for specific heat (equation (29)) to all lunar regolith likely decreases with temperature. However, realistic cases of $x \to 1$ are improbable due to the predominance of glass and other amorphous material in the lunar regolith, so it is reasonable to assume $x \ll 1$.

Shortcomings of this model may arise from its simplicity; it is possible that a more complex damping function is required to accurately model specific heat, that x is not directly equivalent to the crystalline volume fraction of the regolith, or that bulk density has a significant effect at low temperatures. However, this model is presumably an improvement from the previous at lower temperatures, since the temperature-dependent profile of the curve is derived from solid state theory.
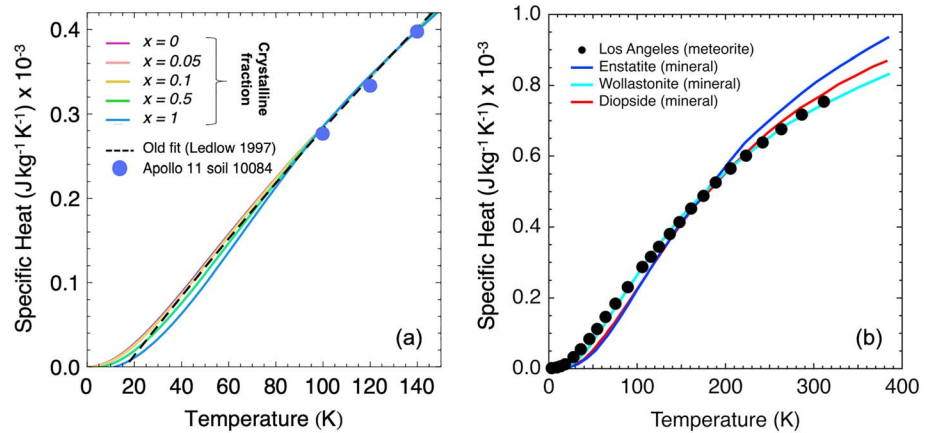
Figure 9. (a) Sensitivity analysis to various degrees of the generic crystalline component (x) of lunar regolith material. Increasing the crystalline volume fraction should slightly lower the specific heat at low temperatures (20–100 K).
(b) For comparison, we show the heat capacity of a shergottite meteorite ("Los Angeles") compared to terrestrial minerals, from the study by Opeil et al. (2012). Low temperature results are remarkably similar to the ones we have derived for the regolith.

4.3. Thermal Conductivity Model

As in the specific heat model, equation (26) can be applied to the two-component linear combination model in the following manner, assuming equal densities of all components:

$$k_{\text{eff}}(T, \rho, p, x) = a(\rho)T^3 + b(\rho)(1-p)[xk_{\text{cr}}(T) + (1-x)k_{\text{am}}(T)] \qquad (30)$$

The temperature-dependent functions of $k_{\text{cr}}(T)$ and $k_{\text{am}}(T)$ are taken from experimental measurements of SiO_2 in the literature (Touloukian & Ho, 1970) and are also fit to high-order polynomials for the highest degree of accuracy. To correctly capture the full variation seen in the laboratory data (shown in Figure 6c) we approximate $k_{\text{cr}}(T)$ and $k_{\text{am}}(T)$ as:

$$k_{\text{am}} = A_{\text{am}} + B_{\text{am}}T^{-4} + C_{\text{am}}T^{-3} + D_{\text{am}}T^{-2} + E_{\text{am}}T^{-1} + F_{\text{am}}T + G_{\text{am}}T^2 + H_{\text{am}}T^3 + I_{\text{am}}T^4$$

and

$$k_{\text{cr}} = A_{\text{cr}} + B_{\text{cr}}T^{-5} + C_{\text{cr}}T^{-4} + D_{\text{cr}}T^{-3} + E_{\text{cr}}T^{-2} + F_{\text{cr}}T^{-1}$$

With values

	Ax	Bx	Cx	Dx	Ex	Fx	Gx	Hx	Ix
k_{am}	-2.03297×10^{-1}	-11.472	22.5793	-14.3084	3.41742	0.01101	2.80491×10^{-5}	3.35837×10^{-8}	-1.40021×10^{-11}
k_{cr}	1.7059	5.10349×10^8	2.971×10^7	1.81897×10^6	1.47654×10^5	2.00771×10^3			

This study will focus on the zeroth-order approximation ($x = 0$), since a quantitative grain-dependent mathematical treatment is beyond our scope, though we will explore sensitively analyses by varying p and x.

Due to the entanglement of the effects of physical properties of regolith (petrologic modes, particle heterogeneity, particle size and shape, etc.) on thermal conductivity, fitting lunar data to equation (30) is nontrivial (e.g., Cremers et al., 1971a, 1971b; Cremers, 1975; Cremers & Hsia, 1973, 1974). Driven by a motivation to understand the effect of bulk density on thermal conductivity, we develop a model based on a well-tested lunar simulant, namely particulate basalt. Measurements from Fountain and West's (1970) study on particulate basalt as functions of density and temperature, discussed previously and shown in Figure 5, are selected as a foundational data set to estimate the constants in equation (30).
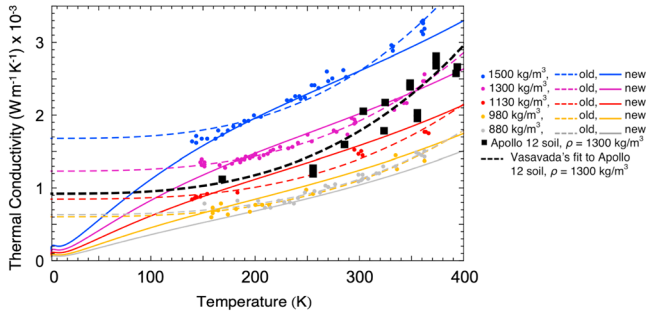
Figure 10. The thermal conductivity of particulate basalt (Fountain & West, 1970) fit to Watson's equation (dotted, labeled "old") as in original publication and fit to equation (32) with constants from equation (32) (solid, labeled "new") at $x = 0$ and $p = 1 - \left(\frac{\rho}{\rho_{basalt}}\right)$. Thermal conductivity of Apollo 12 12001 soil and corresponding fits reported by Vasavada et al. (2012) are reproduced from Figure 3b and plotted in black.

We apply the assumption that $x = 0$ and that the solid conductivity of basalt is a function of the generic amorphous conductivity $k_{am}(T)$. These assumptions are supported by experimental measurements of other extra-terrestrial materials. As shown in Figure 4, most meteoritic basalts (e.g., shergottite Los Angeles and howardite Frankfort) follow amorphous-like thermal conductivity trends (Opeil et al., 2012), and regolith samples include both crystalline and amorphous components. Under these approximations, equation (30) is reduced to

$$k_{eff}(T, \rho, p) = a(\rho)T^3 + b(\rho)(1-p)k_{am}(T) \tag{31}$$

in which a damping constant is absorbed by $b(\rho)$. Finally, this key equation is simultaneously fit to each density in Fountain and West's measurements, namely 880, 980, 1,130, 1,300, and 1,500 kg/m³, using a least squares best fit method to determine functions $a(\rho)$ and $b(\rho)$ (note that 790 kg/m³ measurements are excluded because they are incomplete and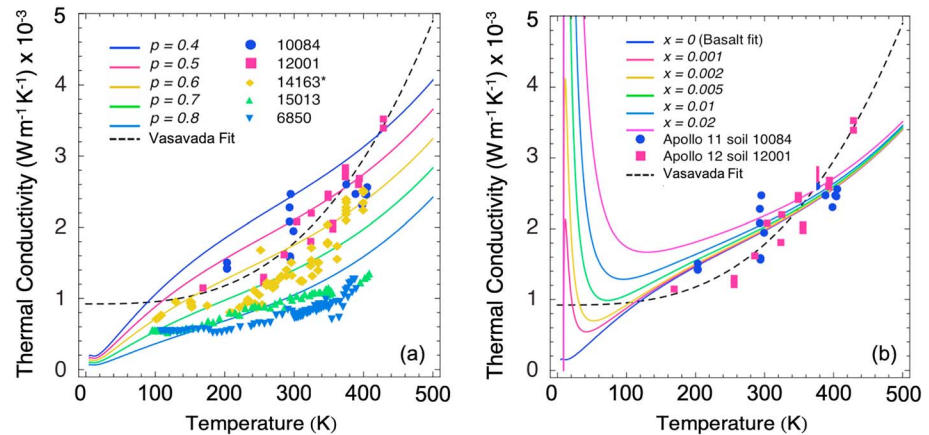 out of our density range of interest). Porosity is taken as $p = 1 - \rho/\rho_{basalt}$ as in equation (14), with the density of basalt assumed to be $\rho_{basalt} = 2,800$ kg/m³. With these coefficients solved, they can be inserted back into equation (31) and applied to lunar regolith of varying densities, and we can study the effects of the degrees of crystalline regolith components on effective thermal conductivity.

4.3.1. Derivation From Simulant Material

A least squares fit from equation (31) applied to Fountain and West's data suggests that $a(\rho)$ is best fit with a constant, such that the radiative component of Watson's equation $k_r = AT^3$ does indeed hold. However, the conductive component, k_c, is found to differ dramatically from previous studies. The best fit for $b(\rho)$ is a second-order polynomial, $B + C\rho^2$, where C is a constant (not to be confused with specific heat, c_V). The final formula and best fit values are given below for reference:

$$
\begin{aligned}
k_{eff}(T, p, p) &= AT^3 + \left(B + Cp^2\right)(1-p)k_{am}(T) \\
A &= 1.3 \times 10^{-11} \, \mathrm{W\,m^{-1}\,K^{-4}} \\
B &= 9.9 \times 10^{-4} \\
C &= 9.2 \times 10^{-10} \, \mathrm{m^6/kg^2}
\end{aligned}
\tag{32}
$$

Figure 10 plots equation (32) (solid lines, labeled "new") with the given coefficients and various bulk densities alongside Fountain and West's (1970) experimental data. For comparison fits are shown to Watson's model with a constant conductive component (dotted lines, labeled "old"). In the measured range 150–400 K, the differences between the old and new models are negligible with respect to the statistical spread and sample size of experimental data.

However, below 150 K the old and new fits begin to deviate significantly. *The thermal conductivities in the new fits are nearly an order of magnitude lower than previously estimated thermal conductivities in the low-temperature regime, most notably at high densities. This is a significant finding for modeling the thermal behavior of the lunar regolith in cold, permanently shadowed regions.* The key difference between this model and previous models is that low temperature values are based on solid state physics and phonon scattering rather than simple extrapolation from higher temperature data. At low temperatures, the traces from the new model more closely resemble the experimental data from meteorites (Figure 4) than do the traces from the old model. The new model may be inaccurate at temperatures above approximately 350 K, but we lack measurements to confirm model fidelity above this temperature.

4.3.2. Application to Lunar Regolith

Figure 10 also overlays the experimental thermal conductivity of Apollo 12 regolith at $\rho = 1,300$ kg/m³ (black squares) and the corresponding fit to Watson's equation (black trace). The standard deviation of measured data points for lunar regolith is much larger than the spread from particulate basalt, indicating a greater experimental uncertainty. The Apollo 12 measurements are fit well by the amorphous end-member approximation curve of the corresponding bulk density of about 1,300 kg/m³ (purple trace).

Figure 11. Sensitivity analysis to (a) various porosities and (b) various generic crystalline components *x*, without a damping constant or peak shift applied.

As a first sensitivity analysis, we vary the porosity *p* of regolith in equation (32) while holding bulk density constant at $\rho = 1{,}300$ kg/m^3 and using the derived constants. This analysis is plotted in Figure 11a. As expected, the thermal conductivity drops with increased porosity. This appears to agree with Opeil et al. (2012) finding that the conductivity varies linearly with inverse porosity in meteorite samples. Results at and below ~20 K in Figure 11a are nonphysical.

As a second sensitivity analysis and thought experiment, we introduce the crystalline component back into equation (31) to estimate its effects on the thermal conductivity in a "first-order approximation." Clearly the variable *x* does not scale one to one with volume fraction of crystalline regolith grains, and a damping or transformation function is likely needed for an accurate model, but *x* is an important qualitative parameter to consider. Figure 11b plots equation (31) with various values of *x*, holding bulk density constant at $\rho = 1{,}300$ kg/m^3 and using the constants from equation (32). The thermal conductivity rises to nonphysical values near what is likely the Debye temperature; this sharp peak is likely nonphysical. *However, a key takeaway is that the thermal conductivity could peak near the Debye temperature when a significant fraction of crystalline grains are present in a lunar regolith sample.*

The results of this second sensitivity analysis are supported by the measurements of meteoritic basaltic rock shown in Figure 4, and in turn help explain the findings of Opeil et al. (2012). Though significantly broader for the meteorite measurements, the peaks near the Debye temperature have a striking resemblance to the peaks in our crystalline sensitivity analysis. Our analysis in this study provides a hypothesis of the thermal conductivity behavior found in Opeil's experiments, as follows. We posit that the drastic increase and subsequent drop in thermal conductivity in the meteorite samples EL and EH is likely due to a significant heat transfer contribution from the crystalline grains within the samples. For the samples in which thermal conductivities increase monotonically with temperature, we expect hypothesize that amorphous grains or at least amorphous-like phonon scattering behavior contributes most. And for the samples with a very broad thermal conductivity peak, there is a trade-off between amorphous-like and crystalline-like behavior.

These findings and accompanying sensitivity analyses demonstrate why measuring real experimental thermal conductivity in the low-temperature and ultralow temperature regimes will be crucial in understanding the thermal properties of the regolith. We acknowledge that intrinsic material properties in the regolith other than bulk density may also have a significant effect on thermal conductivity. Only with experimental confirmation using both lunar simulant and actual regolith samples can we confirm the low-temperature thermal properties of complex multicomponent, polymineralic, polycrystalline, porous regolith material. To further develop the first-order approximation and subsequent models, we suggest an iterative series of experiments and development of new models to better approximate the variables in equations (29) and (32). Due to the complexity of lunar regolith material, it may be of interest to explore machine learning models to predict dependence of thermal properties on the various physical parameters. With the knowledge gained from this study and follow-up experimental and modeling studies, the

planetary science community can derive a more comprehensive model for thermal properties across all relevant temperatures.

5. Application to Lunar Thermal Properties and Discussion

A key prediction of this study is that the thermal conductivity of lunar soil at temperatures below 100 K should be significantly lower than what has been estimated in previous models. The net effect is that heat is less efficiently lost in the cold night, meaning less radiative heat transfer is needed during the day to result in the warm temperatures at depth observed by Apollo (Keihm & Langseth, 1973). Infrared instruments such as the LRO Diviner Lunar Radiometer Experiment can accurately measure surface thermal emission (cf. Figure 1). Interpretation of these measurements with respect to subsurface depth-dependent temperature variations requires a detailed thermal properties model. The biggest unknowns lie in determining temperature as a function of depth below the surface, as well as temporal temperature fluctuations. The findings of this study may influence global models that predict subsurface temperatures on the Moon and other planetary bodies. Namely, this could have a large impact on temperatures simulated by such depth-dependent thermal models in the cold, shadowed, near-polar environments of the Moon, as well as similar ultralow temperature environments in the solar system. Several studies (e.g., Keihm & Langseth, 1973; Vasavada et al., 2012) have shown the standard "Watson's Equation" model to predict both surface and subsurface temperatures near the equator (and Apollo 15 and 17 Heat Flow Experiment sites, 26° and 23°N latitude, respectively). Any new thermal properties model should essentially reproduce the same results as these past models.

However, even at the equator, nighttime surface temperatures can drop below 95 K, so a drop in thermal conductivity in this temperature range could masquerade as radiative heat conduction. The temperature dependence at the high end (>200 K) has been set (e.g., Keihm & Langseth, 1973; Hayne et al., 2017) based on the increase in mean temperature with depth at the Apollo Heat Flow Experiment sites, which requires a large temperature dependence in thermal conductivity.

Essentially, to increase the mean temperature with depth, heat must conduct downward during the hot day faster than it conducts upward in the cold night. If heat loss rates during the cold night are decreased, as we have modeled here, the high-temperature radiative component of heat conduction (e.g., coefficient A in equation (32)) might not need to be as high to produce the same warming.

To demonstrate the implications of our new insights, we have rerun standard thermal models (as in Hayne et al., 2017) for a flat surface at the equator. Figure 12a shows that surface temperatures are approximately reproduced for simulated equatorial illumination, the "zeroth-order" (amorphous end-member) model and Hayne et al., 2017 model. Our thermal conductivity and specific heat capacities are as derived in equations (29) and (32). This study is based on laboratory data, so some discrepancy from the model fit to the lunar surface can be expected. Density profiles, 0.2 "highlands" albedo, and 0.95 infrared emissivity, and 10 mW/m^2 geothermal heat flow are applied for both plots. Figure 12b shows temperatures as a function of depth, the lower temperatures at depth are a result of our fit of coefficient "A" (from equation (32)) to laboratory data (Fountain & West, 1970) as compared to the Hayne et al. (2017) model, which fits subsurface temperatures to the Apollo Heat Flow Experiment and Diviner Surface temperature results. Forcing a fit to Apollo and Diviner is feasible by changing the parameters in equation (32) by roughly a factor of 3, but we have not done so here to create a model consistent with existing laboratory data. This discrepancy between laboratory and in situ data is well known in the literature, but an exhaustive fit to match Diviner and in situ measurements globally (as done in Hayne et al., 2017) is beyond the scope of the work here.

When the models are now run for a simulated polar shadowed environment as shown in Figure 12c, we see two dramatic changes. These models use identical parameters to Figures 12a and 12b except the solar constant is dropped by 3 orders of magnitude from 1,360 to 0.136 W/m^2, which roughly approximates conditions in Cabeus crater (Paige et al., 2010). In this situation we find (1) an increase in the diurnal amplitude and (2) that heat penetrates to far shallower depths and has a much steeper thermal gradient than that predicted by the Hayne et al. (2017) model. This is because the lower thermal inertia at these temperatures will inhibit heat from being stored by the surface and from being transferred to depth.
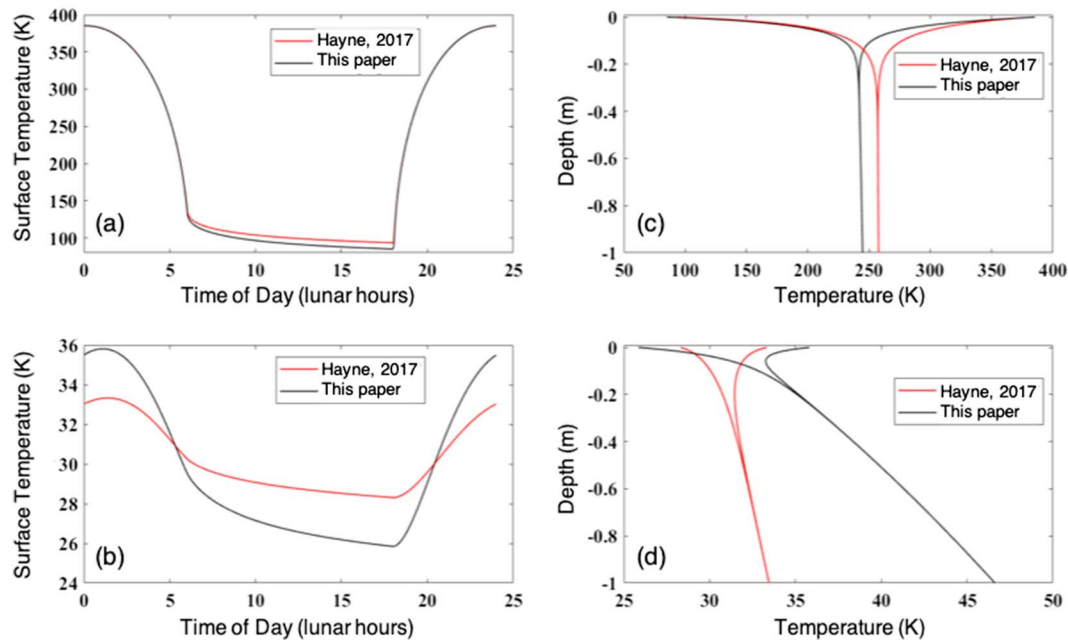
Figure 12. Comparison of the old and new fits input into the Diviner two-layer depth-temperature thermal model, with two standard cases (with 10 mW/m^2 geothermal heat): (a) the equator at noon and (b) simulated polar conditions, that is, the same as (a) but with a solar constant of 0.1361 W/m^{-2}. Model results in panels (c) and (d) show the net effect this has on subsurface temperatures: (c) hints that the existing laboratory data do not provide enough radiative heating to create enhanced temperatures at depth as occurs with in situ lunar regolith (e.g., Hayne et al., 2017; Keihm & Langseth, 1973), while (d) shows that this model will have a large effect on the geothermal gradient in ultracold locations on the Moon.

These changes could help explain the higher than expected diurnal amplitudes observed by the LRO Diviner instrument; however, it has not yet been shown to fully explain the discrepancy. It has also been suggested from the results of multiple observations (Colaprete et al., 2010; Gladstone et al., 2012; Paige et al., 2010) that materials may have lower bulk density in the polar shadowed regions, which would lower the thermal inertia even further, increasing this high-amplitude effect. However, this study suggests that thermal measurements should not be used to directly determine the suspected lower density until the effects of solid state phonon scattering and composition dependence, among other properties, have been accounted for in a thermal model.

The dramatic decrease in penetration of the thermal wave could also imply that volatiles, such as water ice, might be stable at shallower depths than previously thought. At these temperatures of approximately 50 K, compounds such as solid CO_2, SO_2, and even methane clathrate would be stable within approximately 10 cm of the surface (Zhang & Paige, 2009, 2010). This could explain the somewhat surprising detection of highly volatile compounds in near-surface material at the Lunar Crater Observation and Sensing Satellite impact site (Colaprete et al., 2010). At the same time, low thermal conductivities could drive sharper gradients in geothermal heat, which would limit the ultimate depth to which ice could be driven (e.g., Siegler et al., 2011).

Although no known measurements exist, solid water ice crystals likely also exhibit similar temperature-dependent thermal properties as those described in this paper. This could have sweeping applications to many cold ice-dominated bodies in the outer solar system. On such body, the entirety of the crust can be well below 100 K. Such a decrease in thermal conductivity could dramatically slow the rate of heat loss from internal processes (e.g., radioactive decay or serpentinization of a rocky core and tidal heating). Further experimental measurements of silicate and icy planetary materials will be required to address questions raised by this study.

6. Conclusions

This investigation suggests that the current extrapolations widely used in planetary science for both specific heat capacity and thermal conductivity are likely in error below 100 K. At these low temperatures and at

high densities, the current estimates of thermal conductivity may overpredict by an order of magnitude. The models developed here show that a strong dependence of thermal properties on the composition and crystallinity of constituent minerals in regolith material is likely, in particular with amorphous grains exhibiting far lower thermal conductivities than those of crystalline grains at low temperatures. The use of two "generic" phases in these models, namely amorphous and crystalline components derived from SiO_2, are indeed crude estimates. However, this is the closest estimate that can be achieved to date while balancing the complexity of minerology in lunar regolith materials with the limited current knowledge of their experimental thermal properties. Thus, our findings motivate experimental follow-up investigations to determine the temperature dependence of specific heat and thermal conductivity of particulate simulant material of various compositions at low temperatures.

The major conclusions from this work are as follows:

1. A model derived from solid state physics and lunar simulant measurements for heat capacity and regolith thermal conductivity can explain the major features of lunar regolith and meteorite conductivity over the full range of temperatures, in particular at the lowest observed lunar temperatures of approximately 20 K. This contrasts with the previous approach of simply extrapolating higher temperature measurements to low temperatures.
2. The inclusion of newly derived thermal properties at low temperatures (>100 K) appears to lower thermal conductivity by nearly an order of magnitude compared to the previous estimates based on extrapolation.
3. This substantially increases the range of diurnal temperature variations and decreases the depth to which temperature variations penetrate in low temperature regions on the Moon. This may have implications on the depth at which volatiles would be stable from sublimation in such regions.
4. Both density and composition appear to have strong effects on heat capacity and thermal conductivity. It is proposed that most materials relevant to the lunar regolith display "amorphous-like" thermal conductivity behavior, probably due to the prevalence of short-range crystalline defects, small grain sizes, and elevated phonon scattering at grain boundaries. Lunar regolith may generally be coated with fine basaltic glasses, which may dominate conduction across grain boundaries and lead to such "amorphous-like" behavior.
5. The inclusion of the new low-temperature model and the effect of potential compositional variations in the thermal conductivities of lunar regolith affects nighttime temperatures globally.
6. These models are likely to have application to other planetary bodies beyond the Moon, e.g. asteroids and other silicate-dominated objects, and may be intrinsically important to the thermal state and evolution of bodies in the cold outer solar system.

References

Ashcroft, N. W., & Mermin, N. D. (1976). *Introduction to Solid State Physics*. Philadelphia: Saunders.

Aye, K.-M., Paige, D. A., Foote, M. C., Greenhagen, B. T., & Siegler, M. T. (2013). The coldest place on the Moon, Lunar Planet Sci., XLIV, 3016, Houston, Tex.

Birch, A. F., & Clark, H. (1940). The thermal conductivity of rocks and its dependence upon temperature and composition. *American Journal of Science*, *238*(8), 529–558. https://doi.org/10.2475/ajs.238.8.529

Cahill, D. G., & Pohl, R. O. (1988). Lattice vibrations and heat transport in crystals and glasses. *Annual Review of Physical Chemistry*, *39*(1), 93–121. https://doi.org/10.1146/annurev.pc.39.100188.000521

Campbell, G. S., & Norman, J. M. (1998). *An Introduction to Environmental Biophysics*. New York: Springer. https://doi.org/10.1007/978-1-4612-1626-1

Carrier III, W. D., Mitchell, J. K., & Mahmood, A. (1973). The relative density of lunar soil. In Proceedings of the Lunar and Planetary Science Conference (Vol. 4, p. 2403).

Carrier, W. D. I., Olhoeft, G. R., & Mendell, W. (1991). Lunar sourcebook: A user's guide to the Moon. CUP Archive.

Casimir, H. B. G. (1938). Physica 1938, 5, 495. Casimir, H. B. G. Note on the conduction of heat in crystals. *Physica*, *5*(6), 495–500.

Cheng, S. C., & Vachon, R. I. (1969). The prediction of the thermal conductivity of two and three phase solid heterogeneous mixtures. *International Journal of Heat and Mass Transfer*, *12*(3), 249–264. https://doi.org/10.1016/0017-9310(69)90009-X

Colaprete, A., Schultz, P., Heldmann, J., Wooden, D., Shirley, M., Ennico, K., et al. (2010). Detection of Water in the LCROSS Ejecta Plume. *Science*, *330*(6003), 463–468. https://doi.org/10.1126/science.1186986

Cremers, C. J. (1975). Thermophysical properties of Apollo 14 fines. *Journal of Geophysical Research*, *80*(32), 4466–4470. https://doi.org/10.1029/JB080i032p04466

Cremers, C. J., Birkebak, R. C., & White, J. E. (1971a). Lunar surface temperatures at tranquillity base. *AIAA Journal*, *9*(10), 1899–1903. https://doi.org/10.2514/3.50000

Cremers, C. J., Birkebak, R. C., & White, J. E. (1971b). Lunar surface temperatures from Apollo 12. *The Moon*, *3*(3), 346–351. https://doi.org/10.1007/BF00561846

Cremers, C. J., & Hsia, H. S. (1973). Thermal conductivity and diffusivity of Apollo 15 fines at low density. In Proceedings of the Lunar and Planetary Science Conference (Vol. 4, p. 2459).

Cremers, C. J., & Hsia, H. S. (1974). Thermal conductivity of Apollo 16 lunar fines. In Proceedings of the Lunar and Planetary Science Conference (Vol. 5, pp. 2703-2708).

de Vries, D. A. (1963). Thermal properties of soils. In W. R. van Wijk (Ed.), *Physics of Plant Environment*, (pp. 210–236). New York: John Wiley.

Debye, P. (1912). Zur theorie der spezifischen wärmen. *Annalen der Physik*, *344*(14), 789–839. https://doi.org/10.1002/andp.19123441404

Dulong, P. L., & Petit, A. T. (1818). Recherches sur la mesure des températures et sur les lois de la communication de la chaleur. De l'Imprimerie royale.

Einstein, A. (1907). Planck's theory of radiation and the theory of specific heat. *Annalen der Physik*, *22*, 180–190.

Eucken, A. (1911). Über die temperaturabhängigkeit der wärmeleitfähigkeit fester nichtmetalle. *Annalen der Physik*, *339*(2), 185–221. https://doi.org/10.1002/andp.19113390202

Fountain, J. A., & West, E. A. (1970). Thermal conductivity of particulate basalt as a function of density in simulated lunar and Martian environments. *Journal of Geophysical Research*, *75*(20), 4063–4069. https://doi.org/10.1029/JB075i020p04063

Fourier, J. B. J. (1878). *The Analytical Theory of Heat*. Cambridge: The University Press.

Gladstone, G. R., Retherford, K. D., Egan, A. F., Kaufmann, D. E., Miles, P. F., Parker, J. W., et al. (2012). Far-ultraviolet reflectance properties of the Moon's permanently shadowed regions. *Journal of Geophysical Research*, *117*, E00H04. https://doi.org/10.1029/2011je003913

Halajian, J. D., Reichman, J., & Karafiath, L. L. (1967). *Correlation of Mechanical and Thermal Properties of Extraterrestrial Materials*. New York: Bethpage.

Hamilton, R. L., & Crosser, O. K. (1962). Thermal conductivity of heterogeneous two-component systems. *Industrial and Engineering Chemistry Fundamentals*, *1*(3), 187–191. https://doi.org/10.1021/i160003a005

Hayne, P. O., Bandfield, J. L., Siegler, M. A., Vasavada, A. R., Ghent, R. R., Williams, J. P., et al. (2017). Global regolith thermophysical properties of the Moon from the Diviner Lunar Radiometer Experiment. *Journal of Geophysical Research: Planets*, *122*, 2371–2400. https://doi.org/10.1002/2017JE005387

Heiken, G. (1975). Petrology of lunar soils. *Reviews of Geophysics*, *13*(4), 567–587. https://doi.org/10.1029/RG013i004p00567

Hemingway, B. S., Robie, R. A., & Wilson, W. H. (1973). Specific heats of lunar soils, basalt, and breccias from the Apollo 14, 15, and 16 landing sites, between 90 and 350 K. In Proceedings of the Lunar and Planetary Science Conference (Vol. 4, p. 2481).

Horai, K., Winkler, J. L., Keihm, S. J., Langseth, M. G., Fountain, J. A., & West, E. A. (1980). Thermal conduction in a composite circular cylinder: A new technique for thermal conductivity measurements of lunar core samples. *Philosophical Transactions of the Royal Society of London. Series A, Mathematical and Physical Sciences*, *293*(1406), 571–598. https://doi.org/10.1098/rsta.1980.0004

Horai, K. I., & Fujii, N. (1972). Thermophysical properties of lunar material returned by Apollo Missions. *The Moon*, *4*(3-4), 447–475. https://doi.org/10.1007/BF00562011

Horai, K. I., Simmons, G., Kanamori, H., & Wones, D. (1970). Thermal diffusivity and conductivity of lunar material. *Science*, *167*(3918), 730–731. https://doi.org/10.1126/science.167.3918.730

Kannuluik, W. G., & Martin, L. H. (1933). Conduction of heat in powders. *Philosophical Transactions of the Royal Society of London. Series A, Mathematical and Physical Sciences*, *141*(843), 144–158. https://doi.org/10.1098/rspa.1933.0108

Keihm, S. J. (1984). Interpretation of the lunar microwave brightness temperature spectrum: Feasibility of orbital heat flow mapping. *Icarus*, *60*(3), 568–589.

Keihm, S. J., & Langseth Jr, M. G. (1973). Surface brightness temperatures at the Apollo 17 heat flow site: Thermal conductivity of the upper 15 cm of regolith. In Lunar and Planetary Science Conference Proceedings (Vol. *4*, p. 2503).

Kittel, C. (1990). *Introduction to Solid State Physics*. New York: John Wiley.

Laubitz, M. J. (1959). Thermal conductivity of powders. *Canadian Journal of Physics*, *37*(7), 798–808. https://doi.org/10.1139/p59-086

Leadbetter, A. J., & Morrison, J. A. (1963). The low-temperature heat capacities of different forms of SiO 2. *Physics and Chemistry of Glasses*, *4*, 188–192.

Ledlow, M. J., Burns, J. O., Gisler, G. R., Zhao, J. H., Zeilik, M., & Baker, D. N. (1992). Subsurface emissions from Mercury-VLA radio observations at 2 and 6 centimeters. *The Astrophysical Journal*, *384*, 640–655. https://doi.org/10.1086/170906

Lunar Sample Preliminary Examination Team (1969). Preliminary examination of lunar samples from Apollo 11. *Science*, 1211–1227.

McKay, D., Heiken, G., Basu, A., Blanford, G., Simon, S., Reedy, R., et al. (1991). Lunar sourcebook: A user's guide to the Moon. CUP Archive.

Merrill, R. B. (1969). Thermal conduction through an evacuated idealized powder over the temperature range of 100° to 500°K.

Meyer, C. (2012). *The Lunar Sample Compendium*. Houston, TX: Lyndon B. Johnson Space Center (JSC 62905).

Morrison, J. A., & Norton, P. R. (1970). The heat capacity and thermal conductivity of Apollo 11 lunar rocks 10017 and 10046 at liquid helium temperatures. *Journal of Geophysical Research*, *75*(32), 6553–6557. https://doi.org/10.1029/JB075i032p06553

Opeil, C. P., Consolmagno, G. J., & Britt, D. T. (2010). The thermal conductivity of meteorites: New measurements and analysis. *Icarus*, *208*(1), 449–454. https://doi.org/10.1016/j.icarus.2010.01.021

Opeil, C. P., Consolmagno, G. J., Safarik, D. J., & Britt, D. T. (2012). Stony meteorite thermal properties and their relationship with meteorite chemical and physical states. *Meteoritics & Planetary Science*, *47*(3), 319–329. https://doi.org/10.1111/j.1945-5100.2012.01331.x

Paige, D. A., & Siegler, M. A. (2016). New constraints on lunar heat flow rates fro Diviner Lunar Radiometer Experiment polar observations, Lunar Planet. Sci., XLVII. Houston, Tex.

Paige, D. A., Siegler, M. A., Zhang, J. A., Hayne, P. O., Foote, E. J., Bennett, K. A., et al. (2010). Diviner lunar radiometer observations of cold traps in the Moon's south polar region. *Science*, *330*(6003), 479–482. https://doi.org/10.1126/science.1187726

Papike, J. J., Simon, S. B., & Laul, J. C. (1982). The lunar regolith: Chemistry, mineralogy, and petrology. *Reviews of Geophysics*, *20*(4), 761–826. https://doi.org/10.1029/RG020i004p00761

Presley, M. A., & Christensen, P. R. (1997). Thermal conductivity measurements of particulate materials 1. A review. *Journal of Geophysical Research*, *102*(E3), 6535–6549. https://doi.org/10.1029/96JE03302

Robie, R. A., Hemingway, B. S., & Wilson, W. H. (1970). Specific heats of lunar surface materials from 90 to 350 degrees Kelvin. *Science*, *167*(3918), 749–750. https://doi.org/10.1126/science.167.3918.749

Russell, H. W. (1935). Principles of heat flow in porous insulators. *Journal of the American Ceramic Society*, *18*(1-12), 1–5. https://doi.org/10.1111/j.1151-2916.1935.tb19340.x

Schotte, W. (1960). Thermal conductivity of packed beds. *AICHE Journal*, *6*(1), 63–67. https://doi.org/10.1002/aic.690060113

Shkuratov, Y. G., & Bondarenko, N. V. (2001). Regolith layer thickness mapping of the Moon by radar and optical data. *Icarus*, *149*(2), 329–338. https://doi.org/10.1006/icar.2000.6545

Siegler, M. A., Bills, B. G., & Paige, D. A. (2011). Effects of orbital evolution on lunar ice stability. *Journal of Geophysical Research*, *116*, E03010. https://doi.org/10.1029/2010JE003652

Simon, F. (1922). Untersuchungen über die spezifische Wärme bei tiefen Temperaturen. *Annalen der Physik*, *373*(11), 241–280. https://doi.org/10.1002/andp.19223731103

Touloukian, Y., & Ho, C. (1970). In Y. Touloukian, & C. Ho (Eds.), *Thermophys. Prop. Matter-The TPRC Data Ser*. New York: IFI/Plenum.

Vasavada, A. R., Bandfield, J. L., Greenhagen, B. T., Hayne, P. O., Siegler, M. A., Williams, J. P., & Paige, D. A. (2012). Lunar equatorial surface temperatures and regolith properties from the Diviner Lunar Radiometer Experiment. *Journal of Geophysical Research*, *117*, E00H18. https://doi.org/10.1029/2011JE003987

Vasavada, A. R., Paige, D. A., & Wood, S. E. (1999). Near-surface temperatures on Mercury and the Moon and the stability of polar ice deposits. *Icarus*, *141*(2), 179–193. https://doi.org/10.1006/icar.1999.6175

Watson, K. (1964). The thermal conductivity measurements of selected silicate powders in vacuum from 150-350K. California Institute of Technology.

Wechsler, A. E., & Glaser, P. E. (1965). Pressure effects on postulated lunar materials. *Icarus*, *4*(4), 335–352. https://doi.org/10.1016/0019-1035(65)90038-2

Wechsler, A. E., Glaser, P. E., & Fountain, J. A. (1972). Thermal properties of granulated materials. In J. W. Lucas (Ed.), *Thermal Characteristics of the Moon* (Vol. 28, pp. 215–241). Prog. Astronaut. Aeronaut. Cambridge, MA: MIT Press.

Willman, B. M., Boles, W. W., McKay, D. S., & Allen, C. C. (1995). Properties of lunar soil simulant JSC-1. *Journal of Aerospace Engineering*, *8*(2), 77–87. https://doi.org/10.1061/(ASCE)0893-1321(1995)8:2(77)

Woodside, W. M. J. H., & Messmer, J. H. (1961). Thermal conductivity of porous media. I. Unconsolidated sands. *Journal of Applied Physics*, *32*(9), 1688–1699. https://doi.org/10.1063/1.1728419

Zhang, J. A., & Paige, D. A. (2009). Cold-trapped organic compounds at the poles of the Moon and Mercury: Implications for origins. *Geophysical Research Letters*, *36*, L16203. https://doi.org/10.1029/2009gl038614

Zhang, J. A., & Paige, D. A. (2010). Correction to «Cold-trapped organic compounds at the poles of the Moon and Mercury: Implications for origins». *Geophysical Research Letters*, *37*, L03203. https://doi.org/10.1029/2009gl041806

Zeller, R. C., & Pohl, R. O. (1971). Thermal conductivity and specific heat of noncrystalline solids. *Physical Review B: Condensed Matter and Materials Physics*, *4*(6), 2029–2041. https://doi.org/10.1103/PhysRevB.4.2029